Independent activation of ion conduction pores in the double-barreled calcium-activated chloride channel TMEM16A

Novandy K. Lim,* Andy K.M. Lam,* and Raimund Dutzler

Department of Biochemistry, University of Zürich, CH-8057 Zürich, Switzerland

The TMEM16 proteins constitute a family of membrane proteins with unusual functional breadth, including lipid scramblases and Cl^- channels. Members of both these branches are activated by Ca^{2+}, acting from the intracellular side, and probably share a common architecture, which was defined in the recent structure of the lipid scramblase nhTMEM16. The structural features of subunits and the arrangement of Ca^{2+}-binding sites in nhTMEM16 suggest that the dimeric protein harbors two locations for catalysis that are independent with respect to both activation and lipid conduction. Here, we ask whether a similar independence is observed in the Ca^{2+}-activated Cl^- channel TMEM16A. For this purpose, we generated concatenated constructs containing subunits with distinct activation and permeation properties. Our biochemical investigations demonstrate the integrity of concatemers after solubilization and purification. During investigation by patch-clamp electrophysiology, the functional behavior of constructs containing either two wild-type (WT) subunits or one WT subunit paired with a second subunit with compromised activation closely resembles TMEM16A. This resemblance extends to ion selectivity, conductance, and the concentration and voltage dependence of channel activation by Ca^{2+}. Constructs combining subunits with different potencies for Ca^{2+} show a biphasic activation curve that can be described as a linear combination of the properties of its constituents. The functional independence is further supported by mutation of a putative pore-lining residue that changes the conduction properties of the mutated subunit. Our results strongly suggest that TMEM16A contains two ion conduction pores that are independently activated by Ca^{2+} binding to sites that are embedded within the transmembrane part of each subunit.

INTRODUCTION

Calcium-activated chloride channels (CaCCs) constitute a heterogeneous family of membrane proteins, which activate an anion-selective pore in response to the increase of the intracellular calcium concentration (Hartzell et al., 2005; Kunzelmann et al., 2009). Although these proteins have been characterized by electrophysiology for decades (Arreola et al., 1996; Qu and Hartzell, 2000), their molecular identity was unknown for a long time. CaCCs are expressed in different tissues where they contribute to epithelial chloride secretion and electrical signaling in smooth muscle and certain neurons (Huang et al., 2012; Pedemonte and Galietta, 2014). About seven years ago, three groups independently identified the protein TMEM16A (for transmembrane protein of unknown function number 16A) as the main constituent of a CaCC (Caputo et al., 2008; Schroeder et al., 2008; Yang et al., 2008). After activation by Ca^{2+} from the intracellular side with an EC_{50} in the submicromolar range, the protein mediates anion-selective currents (Yang et al., 2008). Activation by Ca^{2+} is voltage dependent with a decreased potency of the ligand at negative transmembrane potentials (Arreola et al., 1996; Kuruma and Hartzell, 2000; Yang et al., 2008; Xiao et al., 2011; Ni et al., 2014). TMEM16A is a member of a conserved family of membrane proteins

that is only expressed in eukaryotic organisms and encompasses 10 paralogues in humans (Schroeder et al., 2008; Yang et al., 2008). Because of assumed molecular features, the name anoctamin was introduced, synonymous for the putative anion selectivity of family members and the presence of eight transmembrane helices predicted by hydropathy analysis (Yang et al., 2008). It was thus unexpected when TMEM16F, another member of the family, was identified as a calcium-activated lipid scramblase, which catalyzes the diffusion of lipids between the two leaflets of the phospholipid bilayer (Suzuki et al., 2010) and thereby leads to the dissipation of the lipid asymmetry and the exposure of the negatively charged phosphatidyl-serine to the cell exterior. The scramblase function was later also observed for other family members (Suzuki et al., 2013), and it was subsequently confirmed for fungal TMEM16 homologues in vitro, after purification and reconstitution of the proteins (Malvezzi et al., 2013; Brunner et al., 2014). Because the two identified CaCCs, TMEM16A and TMEM16B, do not promote lipid scrambling (Malvezzi et al., 2013; Brunner et al., 2014), a functional division within the family was proposed, with some members either functioning as calcium-activated ion channels or

*N.K. Lim and A.K.M. Lam contributed equally to this paper.
Correspondence to Raimund Dutzler: dutzler@bioc.uzh.ch
Abbreviation used: CaCC, calcium-activated chloride channel.
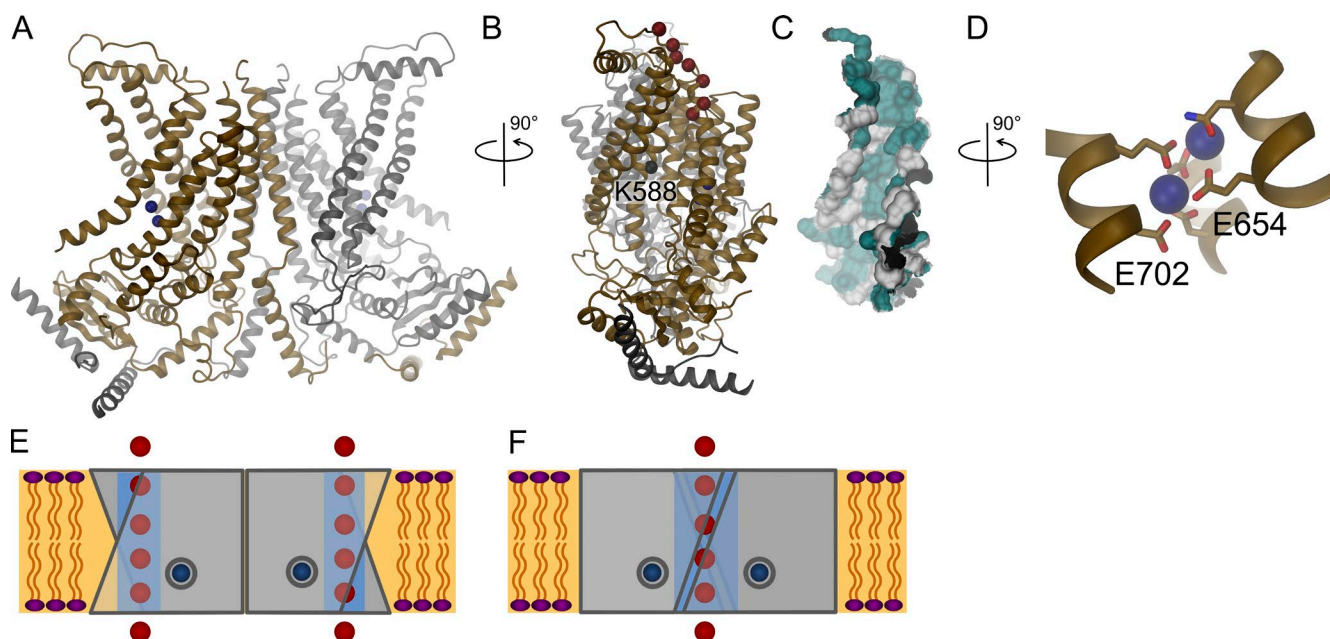
Figure 1. **Structural features of the TMEM16 family.** (A) Ribbon representation of the nhTMEM16 structure. The view is form within the membrane. Bound Ca^{2+} ions are shown as blue spheres. (B) View on the subunit cavity. The relationship to A is indicated. The position of the residue equivalent to Lys588 of mTMEM16 is shown as a black sphere and labeled. Corresponding positions of amino acids that have been shown to change ion conduction in mTMEM16 (Yu et al., 2012) are shown as red spheres. (C) Surface representation of the subunit cavity. The view is as in B. The location of polar and charged residues is shown in cyan. (D) Structure of the Ca^{2+}-binding site. The relation to B is indicated. Ca^{2+} ions are shown as blue spheres, and side chains of interacting residues are shown as sticks. The numbering of selected residues corresponds to mTMEM16A. (E) Schematic representation of TMEM16A containing two pores that are independently regulated by Ca^{2+}. (F) Hypothetical alternative arrangement of subunits resulting in a single pore.

lipid scramblases. Interestingly, some members have also been suggested to possess dual properties (Yang et al., 2012; Picollo et al., 2015). Recently, the architecture of the protein family was revealed by the structure determination of the phospholipid scramblase from the fungus *Nectria haematococca* (termed nhTMEM16; Brunner et al., 2014). Because of the high sequence conservation, it can be assumed that this structure defines the general architecture of both functional branches of the family. The protein forms homodimers, with subunits containing 10 membrane-spanning helices (Fig. 1 A). Each subunit harbors a hydrophilic groove, the "subunit cavity," located at the periphery of the dimer that is exposed to the lipid bilayer (Fig. 1, B and C). This membrane-spanning furrow was proposed to constitute the site for lipid scrambling by offering a hydrophilic path for lipid head groups across the hydrophobic core of the bilayer (Brunner et al., 2014, 2016). The equivalent region in TMEM16 channels is probably involved in ion permeation, as suggested by mutations that affect conduction properties of TMEM16A (Fig. 1 B; Yang et al., 2012; Yu et al., 2012). Each subunit of nhTMEM16 contains a highly conserved calcium-binding site in the vicinity of the subunit cavity, which is embedded within the transmembrane part of the protein (Fig. 1 D; Brunner et al., 2014). The loca-

tion of this site in the hydrophobic part of the phospholipid bilayer offers a plausible explanation for the observed voltage dependence of calcium activation in TMEM16 channels as these divalent cations have to cross part of the transmembrane electric field to reach their binding site (Yu et al., 2012; Brunner et al., 2014; Tien et al., 2014). Mutations of residues constituting the Ca^{2+}-binding site have been shown to affect the activation of both scramblases and channels, suggesting that both functional branches of the family may share a similar mechanism of activation (Yu et al., 2012; Malvezzi et al., 2013; Terashima et al., 2013; Brunner et al., 2014; Tien et al., 2014). Single mutations of Ca^{2+}-binding residues in TMEM16A decrease the potency of Ca^{2+} to a different extent according to their contribution to Ca^{2+} binding and channel activation (Yu et al., 2012; Brunner et al., 2014; Tien et al., 2014). The nhTMEM16 structure thus suggests that family members acting as scramblases contain two potentially independent sites of catalysis, a feature that might also be shared by TMEM16 channels (Fig. 1 E). However, because of the distinct architecture of the subunit cavity, which forms a half-channel that is exposed to lipids on one side, a potential alternative arrangement of subunits in the ion channels TMEM16A and B was envisioned (Brunner et al., 2014). In this alternative arrangement, the two ex-

Independent activation of TMEM16A subunits | Lim et al.

posed half-channels might interact to form a single enclosed aqueous pore that would be completely surrounded by protein residues, akin to other known channel architectures (Fig. 1 F; Doyle et al., 1998; Miyazawa et al., 2003). In such an arrangement, the Ca^{2+}-binding site and the residues lining the ion conduction path would be in close proximity, and it could thus be expected that any change in the pore or the Ca^{2+}-binding site in one of the subunits may affect the activation and conduction properties of the entire protein. In contrast, in the case of two separated ion conduction paths, the same mutation may only affect activation and conduction in one of the two protopores.

We became interested in the question of whether the calcium-activated channel TMEM16A contains two separate ion conduction pores that are independently activated by calcium. In ClC proteins, this question was addressed by the kinetic analysis of single channel recordings (Miller, 1982). However, because the low single-channel conductance of TMEM16A precludes such strategy, we decided to study macroscopic currents of concatenated subunits with one of the two subunits carrying mutations that change the functional properties of the channel. We show that these concatenated proteins are stable and dimeric and that the covalent link between the two subunits does not alter the functional properties of the protein. By introducing mutations that have been shown to shift the potency of Ca^{2+} in nonconcatenated proteins into one subunit, we demonstrate that properties such as the concentration and voltage dependence of activation by Ca^{2+}, as well as the ion selectivity and conductance of the individual protopores are preserved. Our data are thus consistent with functional independence of two ion conduction pores in a double-barreled channel, which resembles the behavior of ion channels of the ClC family.

MATERIALS AND METHODS

Construct generation

The a, c splice variant of mouse TMEM16A (mTMEM16A; Ferrera et al., 2009) was cloned with fragment-exchange (FX) cloning (Geertsma and Dutzler, 2011) into a modified pcDNA3.1 vector (Invitrogen), bearing a 5′ untranslated region (UTR) of hVEGF (from pcDNA4/HisMax; Invitrogen) upstream of the start codon and a 3′ C terminus encoding the Venus YFP, a Myc tag, and a Streptavidin-binding peptide (SBP) tag downstream of the open reading frame. Mutations were made using PCR-based QuikChange mutagenesis (QIAGEN). In the concatemeric constructs, the two monomers were joined by a 31–amino acid–long Gly-Ser linker with sequence GSS GGSGGSGSSGSSGSGSSGGSGGSGSSGS. The two subunits were separately amplified by PCR. The first half of the linker was introduced with the reverse primer of the first subunit and the second half with the forward primer of the second subunit. (Forward primer of the first subunit: 5′-ATATATGCTCTTCTAGTAGGGTCCCCGAGA AGTACTCGACG-3′; reverse primer of the first subunit: 5′-TTATAGCTCTTCATCCACTAGAGCCTGAACTGC CTGATCCACCACTACCTCCGCTCGAGCCCAGCG CGTCCCCATGGTACTCGTA-3′; forward primer of second subunit: 5′-TTATAGCTCTTCAGGAAGTGGTTC GAGTGGAGGTAGTGGTGGATCAGGTTCAAGTGG ATCCAGGGTCCCCGAGAAGTACTCGACG-3′; and reverse primer of the second subunit: 5′-TATATAGCTCTT CATGCCAGCGCGTCCCCATGGTACTCGTA-3′.) The PCR products and the vector were cleaved with SapI (New England Biolabs, Inc.) and subsequently ligated with T4 DNA ligase (New England Biolabs, Inc.). All constructs were confirmed by sequencing.

Protein expression and biochemistry

HEK293T cells were cultured in Dulbecco's modified Eagle's medium (DMEM; Sigma-Aldrich) supplemented with 10 U/ml penicillin, 0.1 mg/ml streptomycin (Sigma-Aldrich), 2 mM L-glutamine (Sigma-Aldrich), and 10% FBS (Sigma-Aldrich) in a humidified atmosphere containing 5% CO_2 at 37°C. For electrophysiology, HEK293T cells were transfected with mTMEM16A constructs at 3 µg DNA per 60-mm culture dish with the calcium phosphate precipitation method (Chen and Okayama, 1987), and medium was changed 4–5 h after transfection. Transfected cells identified by YFP fluorescence were used for patch clamp experiments within 24–72 h of transfection. For biochemical characterization, cells were grown on 10-cm dishes (Corning) to 70–80% cell confluency and transfected with branched polyethylenimine (PEI; Portolano et al., 2014) at a PEI/ DNA ratio of 4:1 (wt/wt) for 36–40 h at 37°C and 2.2% CO_2. After expression, cells were resuspended in buffer A (20 mM HEPES, pH 7.4, 150 mM NaCl, 0.2 mM $CaCl_2$, and 5% [wt/vol] glycerol) containing EDTA-free protease inhibitor complete cocktail (Roche). Cells were lysed with 1% (wt/vol) digitonin (A1905; BioChemica) while stirring for 2 h at 4°C. Insoluble material was pelleted by centrifugation at 40,000 g for 30 min, and the supernatant was incubated with Streptavidin Plus Ultra-Link Resin (Thermo Fisher Scientific) while stirring for 3 h at 4°C. The resin was washed with 30 column volumes of buffer B (buffer A with 0.12% [wt/vol] digitonin), and the bound TMEM16A was eluted with buffer B containing 4 mM biotin. The eluate was concentrated and loaded onto a Zorbax GF450 size-exclusion column (Agilent Technologies) that was equilibrated with buffer B. Fluorescence size-exclusion chromatography (FSEC) was performed with an excitation wavelength of 515 nm and an emission wavelength of 530 nm.

Electrophysiology

All recordings were performed in the inside-out configuration (Hamill et al., 1981). Inside-out patches

were pulled from HEK293T cells expressing the mT-MEM16A construct of interest after the formation of a gigaohm seal. Seal resistance was typically 4–8 GΩ or higher. Recording pipettes were pulled from borosilicate glass capillaries (OD 1.5 mm, ID 0.86 mm; Harvard apparatus or Sutter) and were fire-polished using a microforge (Narishige). Pipette resistance was typically 5–8 MΩ when filled with recording solutions. Voltage-clamp recordings were performed using the Axopatch 200B amplifier controlled by the Clampex 10.6 software through Digidata 1550 (Molecular Devices). For general recordings, raw signals were analogue-filtered through the inbuilt low-pass 4-pole Bessel filter at 5 kHz and were sampled at 10 kHz or higher. For noise analysis, raw signals were low-pass analogue-filtered at 10 kHz with the inbuilt Bessel filter and were sampled at 100 kHz. Liquid junction potential was not corrected. Solution exchange was performed using a theta glass pipette mounted on a high-speed piezo switcher (Siskiyou). Step-like solution exchange was elicited by analogue voltage signals delivered through Digidata 1550. All recordings were performed in symmetrical NaCl solutions except for permeability experiments where the NaCl concentration on the intracellular side was varied (see solution composition). Concentration–response and noise analysis experiments were performed at 80 mV unless specified otherwise. Data were background-subtracted before analysis (background current was obtained by recording in the corresponding 0 Ca^{2+} solution). All experiments were performed at 20°C.

Solutions

Stock Ca-EGTA solution contained 150 mM NaCl, 5.99 mM $Ca(OH)_2$, 5 mM EGTA, and 10 mM HEPES, pH 7.40. Stock EGTA solution contained 150 mM NaCl, 5 mM EGTA, and 10 mM HEPES, pH 7.40. The pH was adjusted using 1 M NMDG-OH solution. The stock Ca-EGTA solution contained a free $[Ca^{2+}]$ of 1 mM. Free $[Ca^{2+}]$ was adjusted by mixing stock Ca-EGTA and EGTA solutions at the ratio calculated according to the WEBMAXC calculator (http://web.stanford.edu/~cpatton/webmaxcS.htm). Free $[Ca^{2+}]$ above 1 mM (up to 3 mM) was adjusted by adding $CaCl_2$ from a 1 M stock solution. The pipette solution (extracellular) had the same ionic composition: 150 mM NaCl and 10 mM HEPES, pH 7.40, and a Ca/EGTA ratio corresponding to free $[Ca^{2+}]$ of 1 µM prepared from the same Ca-EGTA stock solutions. For permeability experiments, NaCl concentrations (with and without Ca^{2+}) were adjusted by mixing NaCl stock solutions and $(NMDG)_2SO_4$ stock solutions at the required ratios. Stock NaCl solutions were the same as above. Stock $(NMDG)_2SO_4$ solutions contained 100 mM $(NMDG)_2SO_4$, 5.99 mM $Ca(OH)_2$, 5 mM EGTA, 10 mM

HEPES, pH 7.40, and 100 mM $(NMDG)_2SO_4$, 5 mM EGTA, and 10 mM HEPES, pH 7.40. In experiments that compare the effect of substitution with $(NMDG)_2SO_4$ or sucrose, the sucrose-based solution had 15 mM NaCl, 280 mM sucrose, and 10 mM HEPES, pH 7.40, with the corresponding Ca-EGTA ratios. In some permeability experiments, the pipette solution had 1 mM $[Ca^{2+}]_{free}$ instead of 1 µM to improve patch stability. We observed no change in ion selectivity in 1 µM and 1 mM $[Ca^{2+}]_{free}$ pipette solutions.

Rundown correction

Significant rundown of the mTMEM16A current occurs in the excised patch configuration, which affects the proper determination of concentration–response relations if left uncorrected. To correct for this rundown, we used a method akin to Ni et al. (2014). A reference Ca^{2+} pulse, typically at submaximal $[Ca^{2+}]_{free}$ (4 µM, 300 µM, or 1 mM), was applied at a regular time interval (17–20 s) before and after the test pulse as programmed in Clampex. The protocol for a typical Ca^{2+} jump experiment is outlined in Fig. S1 A. The magnitude of the test pulse was then normalized to the linearly interpolated, i.e., averaged, magnitude of the pre- and post-reference pulses to obtain a normalized concentration–response relation. This method also allows the construction of concentration–response relations of concatemeric constructs, which span over five orders of magnitude, by merging concentration–response relations recorded separately in the nanomolar and micromolar ranges.

Data analysis

Ca^{2+} activation. For nonconcatemeric constructs that display monophasic activation, concentration–response data were fitted to the Hill equation:

$$I = I_{max} \frac{1}{1 + 10^{((\log EC_{50} - \log[Ca^{2+}])h)}},$$

where EC_{50} is the concentration where the activation is 0.5 and h is the Hill slope. I is normalized to the rundown-corrected current measured at the highest or second to highest Ca^{2+} concentration.

For constructs that display biphasic activation and for comparing concatemeric constructs, concentration–response data were fitted to a biphasic Hill equation:

$$I = I_{max} \left[\begin{matrix} Frac \frac{1}{1 + 10^{((\log EC_{50(1)} - \log[Ca^{2+}])h_1)}} + \\ (1 - Frac) \frac{1}{1 + 10^{((\log EC_{50(2)} - \log[Ca^{2+}])h_2)}} \end{matrix} \right],$$

where I is normalized to the rundown-corrected current measured at the highest or second to highest Ca^{2+} concentration. Frac is the fractional amplitude of the corresponding activation phase.

For the WT_E702Q concatemer, concentration–response data were fitted to a triphasic Hill equation:

Independent activation of TMEM16A subunits | Lim et al.

Table 1. **Fitted parameters from concentration–response experiments**

Construct	Voltage	log EC$_{50(1)}$	EC$_{50(1)}$	h$_1$	log EC$_{50(2)}$	EC$_{50(2)}$	h$_2$	I$_{max}$	Frac
	mV		µM			µM			
WT	80	−6.50 (−6.52 to −6.47)	0.316	1.88 (1.69 to 2.07)	−3.38 (−3.85 to −2.91)	417	0.665 (0.341 to 0.989)	1.46 (1.29 to 1.64)	0.666 (0.566 to 0.766)
	−80	−6.09 (−6.11 to −6.06)	0.813	2.23 (1.98 to 2.47)	−3.38 (−3.85 to −2.91)	417	0.665 (0.341 to 0.989)	1.46 (1.29 to 1.64)	0.666 (0.566 to 0.766)
E702Q	80	−4.41 (−4.46 to −4.36)	38.8	1.09 (0.963 to 1.21)				1.03 (0.996 to 1.06)	
	−80	−3.78 (−3.81 to −3.74)	167	1.19 (1.10 to 1.28)				1.13 (1.10 to 1.16)	
K588E/E702Q	80	−5.03 (−5.08 to −4.97)	9.44	1.01 (0.910 to 1.11)				1.02 (0.987 to 1.06)	
	−80	−4.44 (−4.51 to −4.38)	36	1.07 (0.963 to 1.18)				1.11 (1.05 to 1.17)	
WT_WT	80	−6.68 (−6.71 to −6.65)	0.209	1.60 (1.39 to 1.81)	−3.14 (−3.97 to −2.31)	724	0.511 (0.196 to 0.826)	1.57 (1.24 to 1.89)	0.609 (0.446 to 0.772)
	−80	−6.23 (−6.26 to −6.20)	0.589	1.78 (1.57 to 1.98)	−3.14 (−3.97 to −2.31)	724	0.511 (0.196 to 0.826)	1.57 (1.24 to 1.89)	0.609 (0.446 to 0.772)
WT_E654Q	80	−6.52 (−6.59 to −6.44)	0.302	1.48 (1.18 to 1.77)	−3.76 (−4.03 to −3.49)	174	0.765 (0.304 to 1.22)	1.46 (1.35 to 1.57)	0.653 (0.546 to 0.760)
	−80	−6.11 (−6.16 to −6.05)	0.772	1.76 (1.43 to 2.08)	−3.76 (−4.03 to −3.49)	174	0.765 (0.304 to 1.22)	1.46 (1.35 to 1.57)	0.653 (0.546 to 0.760)
WT_E702Q (biphasic; no constraints)	80	−6.28 (−6.33 to −6.22)	0.525	1.78 (1.45 to 2.12)	−4.12 (−4.18 to −4.06)	75.9	0.851 (0.754 to 0.948)	1.00 (0.978 to 1.02)	0.312 (0.284 to 0.340)
	−80	−5.89 (−5.95 to −5.83)	1.29	1.96 (1.61 to 2.31)	−3.72 (−3.76 to −3.68)	191	1.21 (1.06 to 1.37)	1.00 (0.978 to 1.02)	0.312 (0.284 to 0.340)
WT_E702Q (triphasic; A = 0.6, log EC$_{50(3)}$ = −3.14, h$_3$ = 0.511, h$_1$ = 1.88, h$_2$ = 1.09)	80	−6.26 (−6.31 to −6.21)	0.548	=1.88	−4.21 (−4.29 to −4.13)	61.8	=1.09	1.25 (1.22 to 1.27)	0.517 (0.495 to 0.538)
	−80	−5.92 (−5.97 to −5.87)	1.20	=2.23	−3.77 (−3.82 to −3.72)	171	=1.19	1.41 (1.38 to 1.44)	0.444 (0.424 to 0.463)
WT_E702Q (triphasic; A = 0.6, log EC$_{50(3)}$ = −3.14, h$_3$ = 0.511)	80	−6.29 (−6.34 to −6.23)	0.514	1.88 (1.52 to 2.24)	−4.24 (−4.30 to −4.17)	58	0.921 (0.795 to 1.05)	1.06 (1.04 to 1.07)	0.477 (0.442 to 0.513)
	−80	−5.88 (−5.94 to −5.82)	1.32	1.99 (1.63 to 2.36)	−3.75 (−3.79 to −3.70)	179	1.36 (1.15 to 1.57)	1.06 (1.04 to 1.07)	0.477 (0.442 to 0.513)
K588E_E702Q (biphasic; log EC$_{50(1)}$ = −6.46, h$_1$ = 1.42)	80	= −6.46	=0.347	=1.42	−4.28 (−4.34 to −4.21)	52.5	1.13 (1.01 to 1.24)	1.16 (1.10 to 1.22)	0.015 (0.0055 to 0.024)
	−80				−3.79 (−3.80 to −3.77)	163.2	1.49 (1.44 to 1.55)	1.40 (1.39 to 1.42)	
WT_K588E/E702Q (biphasic)	80	−6.29 (−6.41 to −6.17)	0.513	1.56 (0.811 to 2.30)	−4.20 (−4.61 to −3.79)	63.1	0.616 (0.229 to 1.00)	1.20 (1.08 to 1.31)	0.412 (0.176 to 0.648)
	−80	−5.97 (−6.05 to −5.88)	1.07	1.82 (1.39 to 2.24)	−3.82 (−4.03 to −3.61)	151	1.11 (0.505 to 1.71)	1.15 (1.08 to 1.22)	0.599 (0.506 to 0.692)

Asymptotic 95% confidence intervals are in parentheses; values preceded by = were constrained during fitting; values that are identical at 80 and −80 mV were constrained to a shared but freely varying value; data at 80 and −80 mV were normalized to their respective I$_{max}$ values before global fitting.

$$I = I_{max} \left\{ Frac \left[\frac{A}{1 + 10^{((\log EC_{50(1)} - \log[Ca^{2+}])h_1)}} + \frac{(1-A)}{1 + 10^{((\log EC_{50(3)} - \log[Ca^{2+}])h_3)}} \right] + (1 - Frac)\frac{1}{1 + 10^{((\log EC_{50(2)} - \log[Ca^{2+}])h_2)}} \right\},$$

where A is the fractional component of the high-affinity activation and other parameters are the same as above. Fitting concentration data to this equation therefore accounts for the low-affinity activation observed for the WT subunit (Fig. 3 A) in this concatemer. During curve fitting with this triphasic Hill equation, A, log EC$_{50(3)}$, and h$_3$ were constrained to the corresponding values of the low-affinity phase of the WT_WT concatemer. This leaves the same number of free parameters to be fitted as for the biphasic Hill equation.

We note that in the biphasic and triphasic Hill equations, at least three model parameters (h$_1$, h$_2$, I$_{max}$, and Frac) are interdependent, and thus a rational concern is that the best fit of the parameters may not be accurately estimated. This is of importance, as the second activation often exhibits shallow Hill slope, and hence the plateau of this activation is relatively less well defined than that of nonconcatemeric constructs (see for example Fig. 6 F). More importantly, the interpretation of the relative contribution of the individual subunits in a concatemer requires an accurate estimate of Frac.

Table 2. Fitted parameters from nonstationary noise analysis

Construct	at [Ca^{2+}]	i	γ	$P_{O\,max}$
		pA	*pS*	
WT	2 µM	0.21 ± 0.013	2.63 ± 0.16	0.71 ± 0.022
	1 mM	0.22 ± 0.0091	2.75 ± 0.11	0.87 ± 0.025
E702Q	1 mM	0.19 ± 0.0094	2.38 ± 0.12	0.81 ± 0.018
K588E	2 µM	0.084 ± 0.0057	1.05 ± 0.071	0.48 ± 0.055
K588E/E702Q	1 mM	0.16 ± 0.014	2.00 ± 0.18	0.73 ± 0.025
WT_WT	2 µM	0.15 ± 0.0046	1.88 ± 0.058	0.62 ± 0.039
WT_E654Q	2 µM	0.17 ± 0.018	2.13 ± 0.23	0.66 ± 0.015
	1 mM	0.196 ± 0.019	2.45 ± 0.24	0.81 ± 0.024
WT_E702Q	2 µM	0.14 ± 0.0084	1.75 ± 0.11	0.50 ± 0.037

Presented as mean ± SEM calculated from fitted parameters from individual patches.

To improve the quality of the fits, the activation curves obtained at 80 and −80 mV were fitted simultaneously where Frac and I_{max} were constrained, respectively, to a shared but freely varying value whenever possible. For the WT_E702Q concatemer, good estimates of these model parameters can be obtained without imposing specific constraints. The asymptotic 95% confidence intervals of the log EC_{50} of the first and second activation are generally narrow as the log EC_{50} values show little correlation with the other free parameters and are well defined by the data. The asymptotic 95% confidence intervals of the other fitted parameters (h_1, h_2, I_{max}, and Frac) are higher, but still smaller than 20% of the best-fit values. We have also characterized the errors in parameter estimation during curve fitting by basic Monte Carlo simulation using the root mean squared errors (RMSEs) and the best-fit parameters, assuming that the errors follow a Gaussian distribution with a mean of zero (Fig. S2; see legend for details). We found that, given the experimental errors, well-defined distributions in the expected range can be obtained for all six free parameters for both voltages (Fig. S2 A). Similar to the asymptotic 95% confidence interval, which is symmetric, the distributions of all fitted parameters are also approximately symmetric, with that of h_1 being slightly skewed for both voltages. Correlations between Frac and h_1, h_2, and I_{max} are also observed (Fig. S2, B and C), but the values are expected to cluster around the peaks of the distributions. Thus, although the precise values of these parameters cannot be uniquely determined, they represent reliable estimates. For comparison, we have also included the best fit with h_1 and h_2 constrained to the corresponding values of the nonconcatemeric constructs, which yielded very similar best-fit values (Table 1).

For the K588E_E702Q concatemer, the fraction of the first activation is very small compared with that of the second activation, and as a result, the first activation cannot be fitted very well. For this reason, we have constrained both log $EC_{50(1)}$ and h_1 to the best-fit values obtained for WT_E702Q to obtain an acceptable asymptotic 95% confidence interval for the remaining parameters. The constrained log $EC_{50(1)}$ and h_1 were further adjusted manually. For the WT_K588E/E702Q concatemer, the asymptotic 95% confidence intervals of h_1, h_2, I_{max}, and Frac are somewhat wider than that of WT_E702Q when all the parameters are allowed to vary freely. However, the best-fit values, using our simulation results as a guide, also represent reliable estimates in this setting.

For presentation, the data were normalized to the estimated I_{max} and were fitted with I_{max} constrained to 1. Details of the parameters and constraints can be found in Table 1.

Nonstationary noise analysis. Nonstationary noise analysis was performed according to Sigworth (1980). Nonstationary noise analysis requires information on the fluctuation, characterized by its variance, of an activating and/or deactivating current that samples the mean current space available to the channel. The fluctuation is not time dependent per se but appears to be dependent on time only because P_O is time dependent. This information was experimentally obtained by periodically pulsing Ca^{2+} on the intracellular side at saturating concentrations in concentration jump experiments so that the variance of the mean current at each time point could be estimated. For an example, see Fig. S1 B. Digitized data were filtered at 7.5 kHz with a low-pass Gaussian filter (Clampfit; Molecular Devices) and were subsequently decimated fourfold to a final sampling frequency of 25 kHz before analysis. The variance of 50–100 aligned, successive and kinetically identical currents at each time point was computed using the successive difference method proposed by Heinemann and Conti (1992), which allows the calculation of the variance in the presence of current rundown and artifacts arising from step-like solution switching. The computed variance was plotted against the mean current, and the data were fitted to

$$\text{Variance} = i\langle I \rangle - \frac{\langle I \rangle^2}{N} + c,$$

Independent activation of TMEM16A subunits | Lim et al.

where $\langle I \rangle$ is the mean current, i is the single-channel current, N is the number of functional channels that can contribute to the observed fluctuation, and c is the background variance. The background variance that was estimated from the fit was subtracted, and the resulting data were refitted to the same equation without the background term c. With data that display a parabolic shape, it is possible to obtain a meaningful estimate of the maximum P_O as N is well defined. We therefore estimated the maximum P_O from the ratio of the maximal mean current to the nonzero x-intercept, which corresponds to the theoretically achievable maximal mean current if P_O was 1. With data that do not reach a maximum, N cannot be estimated reliably, and thus the estimated maximum P_O, which is <0.5, rather represents an upper limit. The single-channel current i can generally be estimated with higher confidence, as it is the slope at the zero x-intercept, which is usually well defined by the data.

For presentation, the pairs of variance and $\langle I \rangle$ data points were sorted, reduced, and smoothed using the substitute average method. The variance-$\langle I \rangle$ plots from individual patches were normalized to the estimated $\langle I \rangle_{max}$ such that the ordinate becomes variance/$\langle I \rangle_{max}$ and the abscissa becomes P_O. The resulting plots from the individual patches were then merged and reduced using the substitute average method.

Data analysis and statistics. Data analysis was performed using Clampfit, Excel (Microsoft), and Prism 5 and/or 6 (GraphPad Software). Curve fitting and statistical analysis were performed in Prism 5 and/or 6. For comparison of two samples, statistical differences were detected using the t test and were considered significant when $P < 0.05$. Data are presented as mean ± SEM. Parameters obtained from curve fitting shown in Table 1 are presented as the best-fit value together with the asymptotic 95% confidence intervals, whereas those in Table 2 are presented as mean of the individual fits ± SEM.

Online supplemental material

Fig. S1 shows measurement protocols and reversal potential measurements. Fig. S2 shows errors in parameter estimation during curve fitting to the triphasic Hill equation estimated in a Monte Carlo simulation for the WT_E702Q concatemer at 80 and −80 mV.

RESULTS

Biochemical characterization of concatemeric proteins

To address the question of whether TMEM16A comprises two ion conduction pores that are independently activated by Ca^{2+}, we have generated concatenated constructs that either contained two WT subunits (WT_
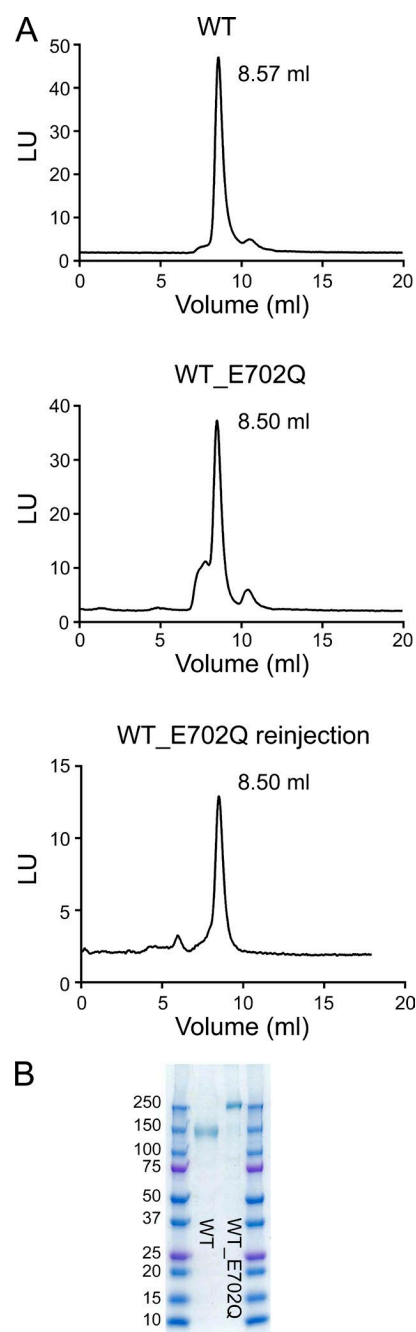
Figure 2. **Purification and biochemical characterization of mTMEM16 constructs.** (A) Gel filtration profiles of WT and the WT_E702Q concatemer. WT (top) and WT_E702Q (center) loaded after purification in digitonin. The protein was detected by the fluorescence of the YFP tag. The bottom graph shows a reinjection of the main peak fraction of WT_E702Q. The elution volume is indicated. LU, luminescence units. (B) SDS-PAGE of the purified proteins. Both proteins (WT and WT_E702Q) run at the expected molecular weight. Molecular weights of the markers (kilodaltons) are indicated.

WT) or a combination of WT and point mutants with altered properties (e.g., WT_E702Q). These constructs were prepared by linking the C terminus of one to the N terminus of another subunit via a 31-residue-long
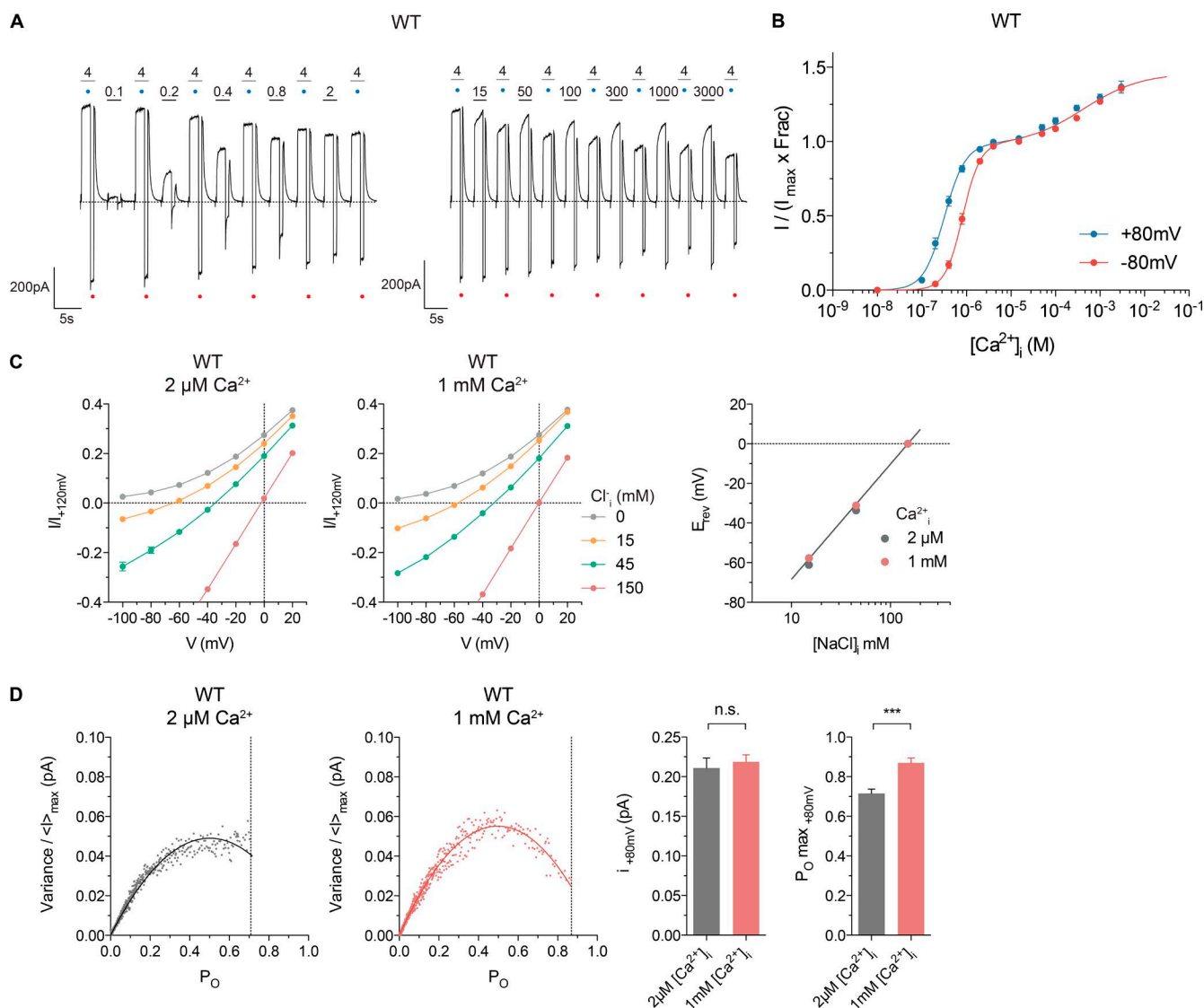
Figure 3. **Functional properties of WT mTMEM16A.** (A) Representative currents of WT mTMEM16A at 80 and −80 mV. Numbers show $[Ca^{2+}]_{free}$ (µM) on the intracellular side of the excised patch. Each sweep was recorded using the voltage and piezo protocol shown in Fig. S1 A. Individual sweeps are separated by a regular time interval (17–20 s, programmed in Clampex) and are concatenated to form a single trace. Blue and red dots indicate the reference pulses used for rundown correction at 80 and −80 mV, respectively (see Materials and methods). Currents at low (left) and high Ca^{2+} (right) were recorded from different patches. (B) Rundown-corrected concentration–response relations of WT mTMEM16A at 80 and −80 mV (n = 4–12 for each data point). Lines are the best fit to a biphasic Hill equation. (C) Na^+ versus Cl^- selectivity of WT mTMEM16A. I-V plots of the instantaneous current in response to the indicated voltage steps at 150 mM extracellular and the indicated intracellular NaCl concentrations at 2 µM (n = 6, left) and 1 mM (n = 6–7, middle) $[Ca^{2+}]_{free}$. Data are mean values of normalized I-V plots from individual patches unless otherwise stated. (right) Relation between intracellular [NaCl] and reversal potential (E_{rev}) at 2 µM (n = 6) and 1 mM (n = 6–7) $[Ca^{2+}]_{free}$. The line indicates the Nernst potential of Cl^-. (D) Merged and averaged variance-<I> plots of WT mTMEM16A obtained at 2 µM (n = 21, left) and 1 mM (n = 10, middle) $[Ca^{2+}]_{free}$ at 80 mV. The solid lines are the best fit to the noise parabola equation. Dotted lines indicate the mean $P_{O\,max}$ across patches. Other variance-<I> plots were constructed in the same way unless otherwise stated. (right) Pooled data of individual i and $P_{O\,max}$ values obtained from individual patches expressing WT mTMEM16A at 2 µM (n = 21) and 1 mM (n = 10) $[Ca^{2+}]_{free}$. n.s., P > 0.05; ***, P ≤ 0.001. In B–D, data are presented as mean and errors as SEM.

linker consisting of alternating Gly and Ser residues. The second subunit in the concatemer is appended by a C-terminal YFP to facilitate the detection of the protein. We have subsequently investigated whether the concatenated proteins are properly folded and assembled and whether their biochemical properties resemble TMEM16A. Both the YFP-tagged WT_E702Q concatemer and a TMEM16A-YFP fusion (WT) used for functional characterization appear to predominantly localize at the plasma membrane when expressed in HEK293 cells. When purified in the detergent digitonin and loaded on a gel-filtration column, WT_E702Q

Independent activation of TMEM16A subunits | Lim et al.

elutes similarly to WT, at a volume that is compatible with a dimeric organization of the protein (Fig. 2 A). Upon subjection to SDS-PAGE analysis, the concatenated protein migrates at twice the size of a single subunit and no proteolysis is observed, indicative of a stable protein (Fig. 2 B). Collectively, these results suggest that the covalent linkage neither affected the stability of the protein nor did it change its oligomerization behavior, which could have been the case if instead of an intramolecular dimerization, the subunits in the linked concatemer would favor intermolecular interactions, thereby generating assemblies of larger size.

Functional properties of WT

For the functional characterization of TMEM16A constructs, we expressed unlinked and concatenated proteins in HEK293 cells and investigated their properties by electrophysiology in excised patches in the inside-out configuration (Tables 1 and 2). We first studied the properties of WT in a broad range of Ca^{2+} concentrations. At submicromolar concentrations, the protein shows the previously described steep activation that reflects the cooperative opening of the ion conduction pore (Fig. 3, A and B; Arreola et al., 1996; Kuruma and Hartzell, 2000; Yang et al., 2008). In this concentration range, the activation by Ca^{2+} is voltage dependent, with a decreased potency of the ligand at negative potentials (Fig. 3 B). Between 2 and 100 µM Ca^{2+}, the current levels remain constant until, at higher concentrations, a second smaller activation step is observed (Fig. 3, A and B). This biphasic activation is only evident upon a careful correction of the irreversible rundown that becomes more severe at higher Ca^{2+} concentration, and it might thus have escaped previous detection. The second component is shallow, it increases the currents measured in the first plateau by ~25%, and it saturates with an apparent EC_{50} of 417 µM (Fig. 3 B and Table 1). Unlike the first activation, the second activation step is not voltage dependent (Fig. 3 B). We were interested in whether the activation at high Ca^{2+} concentrations changes the permeation properties of the channel, as it has been suggested previously (Kuruma and Hartzell, 2000; Schroeder et al., 2008; Peters et al., 2015), or whether it reflects an increase in the open probability with similar ion conduction characteristics. We thus studied the ion selectivity of the channel by quantifying reversal potentials (E_{rev}) in asymmetric conditions and its conductance (γ) and open probability (P_O) by nonstationary noise analysis at low and high Ca^{2+} concentrations. The currents measured from channels activated at low (1–2 µM) Ca^{2+} in a 10-fold NaCl gradient (c_{out} 150 mM, c_{in} 15 mM) with an osmotic compensation of the low salt intracellular solution by sucrose reverse at about −45 mV (Fig. S1 C). This value is consistent with a previous study and was attributed to an imper-

fect selectivity for anions over cations (Qu and Hartzell, 2000). However, when replacing sucrose by NMDG sulfate to minimize junction potential changes (see companion paper by Jeng et al. in this issue) in the same 10-fold NaCl gradient, E_{rev} approaches the Nernst potential of Cl^- (i.e., −58 mV), which indicates that the anion selectivity of the channel might be stronger than anticipated (Fig. 3 C). This was also previously suggested based on data obtained from purified and reconstituted TMEM16A (Terashima et al., 2013). We repeated the selectivity experiments at 1 mM Ca^{2+} and measured a very similar E_{rev}, thus suggesting that the anion over cation selectivity of the channel did not change in conditions where we observed the second activation step (Fig. 3 C). To further characterize the functional properties of the channel, we performed nonstationary noise analysis after the rapid exposure to 2 µM and 1 mM Ca^{2+} (Fig. 3 D and Fig. S1 B). Fitting the variance of the current as a function of the mean current amplitude to the noise parabola equation allows an estimation of γ and P_O of the channel (see Materials and methods). At both Ca^{2+} concentrations, we have observed a parabolic relationship that allowed for a reliable fit of both parameters (Fig. 3 D and Table 2). Interestingly, the estimate of γ of ~2.7 pS is very similar at both Ca^{2+} concentrations, whereas P_O of the channel is ~20% higher when measured at 1 mM than at 2 µM Ca^{2+} (Fig. 3 D). This increase in P_O is consistent with the increment observed for macroscopic currents (Fig. 3 B). The fitted values are in general agreement with a previous analysis of TMEM16A (Ta et al., 2016). Our data thus suggest that the increase in current in WT at high Ca^{2+} concentrations might result from an increase in P_O without strongly affecting the permeation properties of the pore.

Functional properties of WT_WT

We next investigated whether the concatenated WT_WT protein has retained a similar functional behavior as WT. We thus repeated the same experiments used to characterize the functional properties of WT for this concatenated construct. The dose–response relationships show a very similar biphasic activation as observed for WT, with a cooperative voltage-dependent opening at low Ca^{2+} concentrations and a shallow voltage-independent second component at high Ca^{2+} concentrations (Fig. 4, A and B; and Table 1). As for WT, the WT_WT currents are highly Cl^- selective at low and high Ca^{2+} concentrations (Fig. 4 C), and both γ and P_O estimated by noise analysis at 2 µM Ca^{2+} closely resemble the values measured for WT (Fig. 4 D and Table 2). Collectively, our data strongly suggest that the covalent linkage of the two subunits in the dimeric protein did not significantly affect the ion permeation and gating characteristics of the protein.
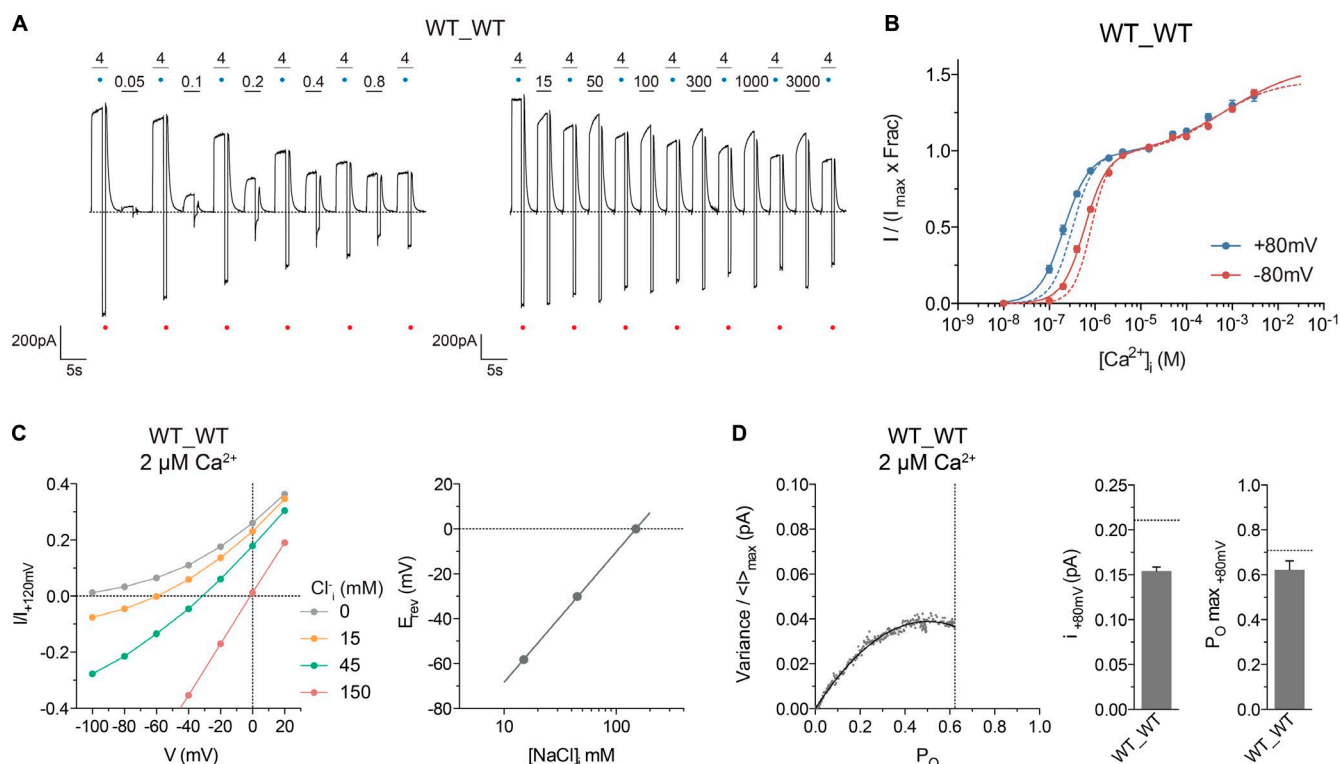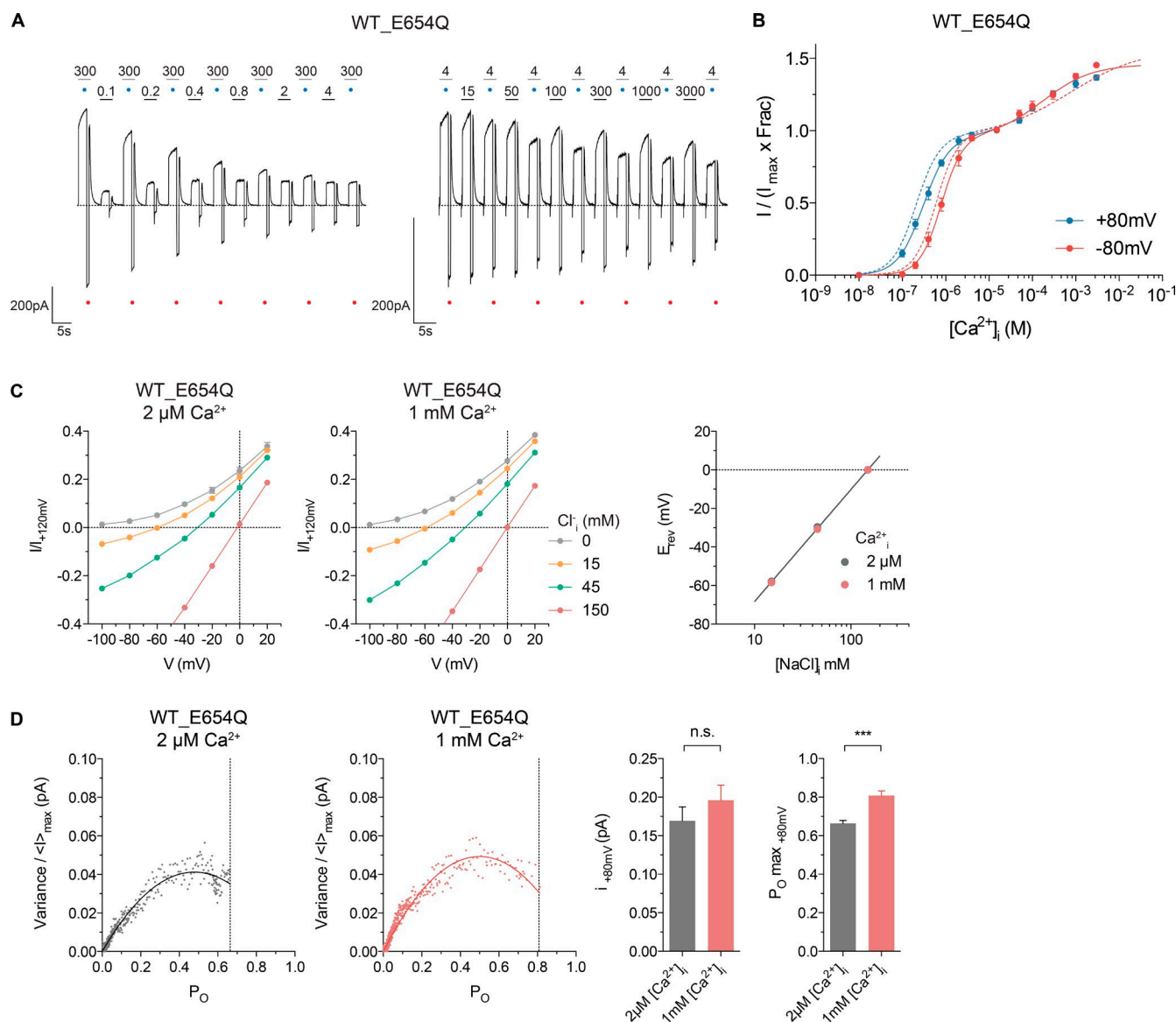
Figure 4. **Functional properties of the WT_WT concatemer.** (A) Representative currents of the WT_WT concatemer at 80 and −80 mV. Blue and red dots indicate the reference pulses used for rundown correction at 80 and −80 mV, respectively (see Materials and methods). (B) Rundown-corrected concentration–response relations of the WT_WT concatemer at 80 and −80 mV (n = 8–11 for each data point). Lines are the best fit to a biphasic Hill equation. Dashed lines indicate the relations of WT mTMEM16A at 80 and −80 mV. (C) Na$^+$ versus Cl$^-$ selectivity of the WT_WT concatemer. (left) I-V plots recorded at 150 mM extracellular and the indicated intracellular NaCl concentrations at 2 µM (n = 6) [Ca^{2+}]$_{free}$. (right) Relation between intracellular NaCl concentration and E$_{rev}$ at 2 µM (n = 6) [Ca^{2+}]$_{free}$. The line indicates the Nernst potential of Cl$^-$. (D, left) Merged and averaged variance-<I> plots of the WT_WT concatemer obtained at 2 µM (n = 5) [Ca^{2+}]$_{free}$ at 80 mV. The dotted line indicates the mean P$_{O max}$ across patches. (right) Pooled data of individual i and P$_{O max}$ values obtained from individual patches expressing the WT_WT concatemer at 2 µM (n = 5) [Ca^{2+}]$_{free}$. Dotted lines indicate the corresponding value of WT mTMEM16A. In B–D, data are presented as mean and errors as SEM.

A concatemer containing a subunit with compromised activation properties

Because the concatenation of two subunits did not strongly affect protein function, we were interested whether the functional phenotype of WT would be preserved in the context of a covalently linked heterodimer, where one of the two subunits contains a mutation that impedes Ca^{2+} activation. This would only be expected in the case of two functionally independent pores in the dimeric protein. For this purpose, we generated a concatenated protein consisting of a WT subunit followed by a second subunit containing the mutation E654Q (WT_E654Q) in the Ca^{2+}-binding site, for which we and others have previously not observed significant activity at Ca^{2+} concentrations up to 1 mM (Brunner et al., 2014; Tien et al., 2014). The Ca^{2+} dose–response relationships show a very similar biphasic activation that was also observed for WT and WT_WT, with a predominant activation at low and a second shallow step at high Ca^{2+} concentrations (Fig. 5,

A and B; and Table 1). Because the second component is voltage independent with properties that resemble WT and WT_WT, we assume that any contribution of the subunit containing the E654Q mutant is small. At low Ca^{2+} concentrations, activation proceeds with an EC$_{50}$ that is very close to WT (Fig. 5 B and Table 1). Similarly, the voltage dependence of this Ca^{2+} activation is preserved in this construct (Fig. 5 B). The steep dependence on Ca^{2+} with a Hill coefficient consistently above one indicates that the cooperativity of opening is an intrinsic property of a single subunit (Table 1). Like in WT, the currents are highly anion selective at both low and high Ca^{2+} concentrations (Fig. 5 C). Finally, as suggested by our noise analysis, the channel shows very similar properties as WT with an increase in P$_O$ at high Ca^{2+} concentrations (Fig. 5 D). The results from WT_E645Q, which only contains one functional subunit, are thus consistent with a dimeric protein comprising two ion conduction pores that are independently activated by Ca^{2+}.

A

WT_E654Q

B

WT_E654Q

C

D

Figure 5. **Functional properties of the WT_E654Q concatemer.** (A) Representative currents of the WT_E654Q concatemer at 80 and −80 mV. Blue and red dots indicate the reference pulses used for rundown correction at 80 and −80 mV, respectively (see Materials and methods). (B) Rundown-corrected concentration–response relations of the WT_E654Q concatemer at 80 and −80 mV (n = 4–10 for each data point). Lines are the best fit to a biphasic Hill equation. Dashed lines indicate the relations of WT_WT at 80 and −80 mV. (C) Na$^+$ versus Cl$^-$ selectivity of the WT_E654Q concatemer. (left and middle) I-V plots recorded at 150 mM extracellular and the indicated intracellular NaCl concentrations at 2 μM (n = 6) and 1 mM (n = 6–7) [Ca^{2+}]$_{free}$. (right) Relation between intracellular [NaCl] and E$_{rev}$ at 2 μM (n = 6) and 1 mM (n = 6–7) [Ca^{2+}]$_{free}$. The line indicates the Nernst potential of Cl$^-$. (D, left and middle) Merged and averaged variance-<I> plots of the WT_E654Q concatemer obtained at 2 μM (n = 6) and 1 mM (n = 8) [Ca^{2+}]$_{free}$ at 80 mV. The dotted lines indicate the mean P$_{O max}$ across patches. (right) Pooled data of individual i and P$_{O max}$ values obtained from individual patches expressing the WT_E654Q concatemer at 2 μM (n = 6) and 1 mM (n = 8) [Ca^{2+}]$_{free}$. n.s., P > 0.05; ***, P ≤ 0.001. In B–D, data are presented as mean and errors as SEM.

A concatemer containing a subunit with decreased potency for Ca^{2+}

In the next step, we wanted to characterize the functional behavior of a concatenated protein containing two functional subunits that are activated at different Ca^{2+} concentrations. We thus combined WT with the mutant E702Q (WT_E702Q), which also removes a negatively charged residue from the Ca^{2+}-binding site. The

same construct was used for the biochemical characterization of the concatemeric protein (Fig. 2). E702Q itself mediates robust currents (Fig. 6 A) but has an EC$_{50}$ that is 122-times higher (i.e., from 0.32 μM in WT to 39 μM in E702Q when measured at 80 mV; Yu et al., 2012; Brunner et al., 2014; Tien et al., 2014) and somewhat reduced cooperativity compared with WT (Fig. 6 B and Table 1). As for WT, Ca^{2+} activation is voltage de-
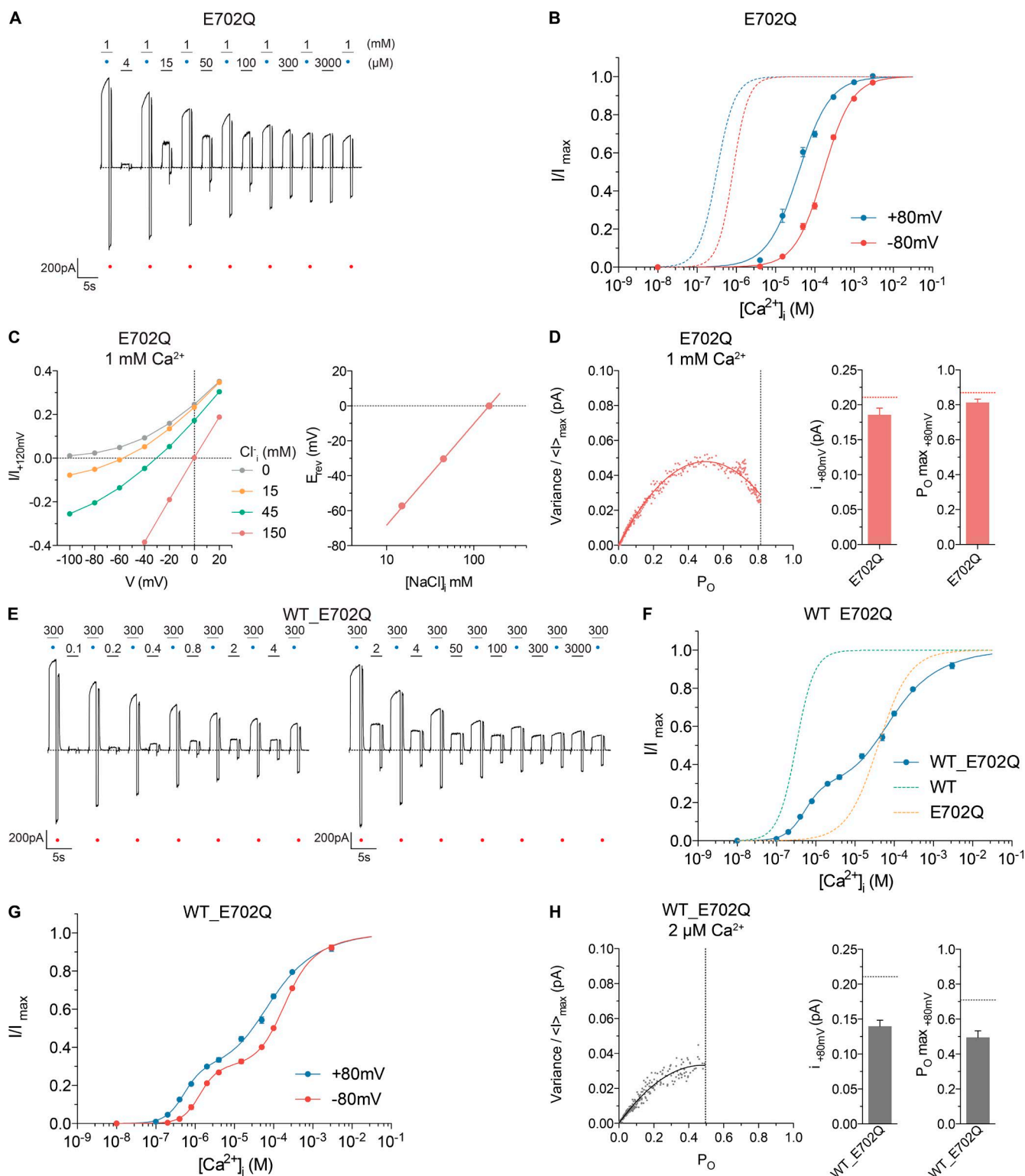
Figure 6. **Functional properties of the WT_E702Q concatemer.** (A) Representative currents of the E702Q mutant at 80 and −80 mV. (B) Rundown-corrected concentration–response relations of the E702Q mutant at 80 and −80 mV (n = 13–14 for each data point). Solid lines are the best fit to the Hill equation. Dashed lines indicate the relations of WT mTMEM16A at 80 and −80 mV. (C) Na$^+$ versus Cl$^-$ selectivity of the E702Q mutant. (left) I-V plots recorded at 150 mM extracellular and the indicated intracellular NaCl concentrations at 1 mM (n = 5) [Ca^{2+}]$_{free}$. (right) Relation between intracellular [NaCl] and E_{rev} at 1 mM (n = 5) [Ca^{2+}]$_{free}$. The line indicates the Nernst potential of Cl$^-$. (D) Merged and averaged variance-<I> plot and pooled data (n = 10) of the E702Q mutant obtained at 1 mM [Ca^{2+}]$_{free}$ at 80 mV. (E) Representative currents of the WT_E702Q concatemer at 80 and −80 mV. (A and E) Blue and red dots indicate the reference pulses used for rundown correction at 80 and −80 mV, respectively (see Materials and methods).
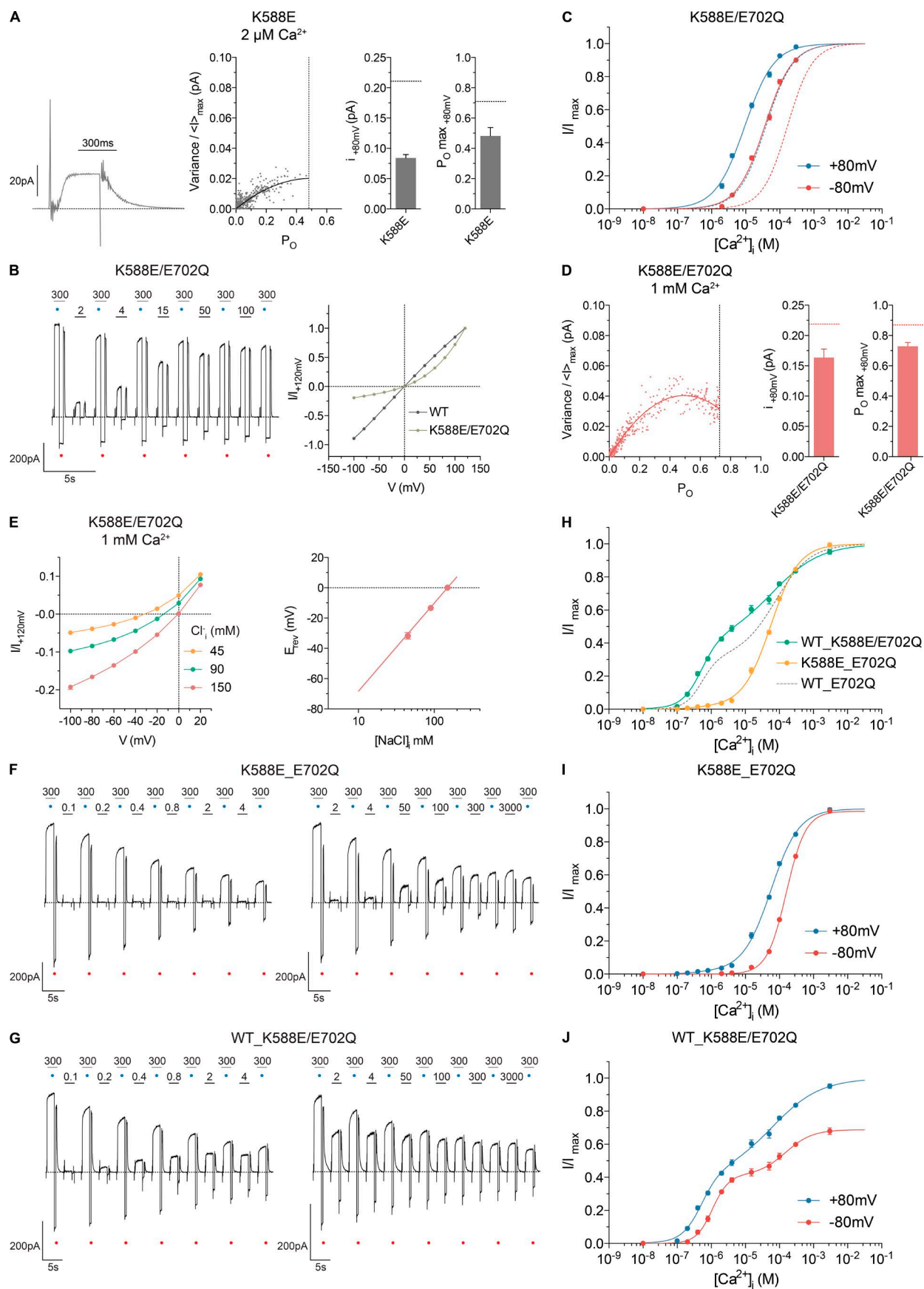
pendent with a decreased potency at negative potentials (Fig. 6 B). Unlike WT, we did not, in this case, observe a biphasic activation, but we cannot exclude that the second component might either be hidden in the main activation step or shifted to very high Ca^{2+} concentrations. Similar to WT, the currents (activated at 1 mM Ca^{2+}) reverse close to the Nernst potential of Cl^-, indicative for a highly anion-selective channel (Fig. 6 C). Because noise analysis of this (nonconcatemeric) mutant suggested a similar γ and P_O as WT (Fig. 6 D), we expected to observe a biphasic activation of the WT_E702Q concatemer with two similar current levels. This behavior should be easily distinguishable from the biphasic activation of WT because, compared with the second component of WT, the activation of the E702Q subunit proceeds at an 11-times-lower Ca^{2+} concentration, contributes about equally to the total currents, and is voltage dependent. Conversely, we anticipate the high Ca^{2+} component of WT to be hidden in the dominant activation of the E702Q subunit. The predicted behavior, with separate transitions at low and high Ca^{2+} concentrations, can readily be observed in the dose–response relationships of this construct (Fig. 6, E and F). As expected, both activation steps are voltage dependent (Fig. 6 G). To account for the biphasic activation of the WT subunit, a sum of three Hill equations was used to fit the WT_E702Q dose–response data (see Materials and methods). We obtained EC_{50} values that are very close to the values of the respective nonconcatenated homomeric proteins (Fig. 6 E and Table 1), either with only four free parameters where h_1 and h_2 were both constrained or six free parameters where h_1 and h_2 were allowed to vary. Consistent with our expectation, we observed in both fits that both transitions contribute about equally to the total currents with a Frac value of ~0.5 (Fig. 6 E and Table 1). Moreover, when allowed to be further optimized, the values of both h_1 and h_2 remain very similar to their respective nonconcatenated counterparts. In the latter case where six free parameters were to be fitted, we have investigated the interdependence of the parameters by simulations to ensure the reliability of the fit (Fig. S2 and Materials and methods). In addition, we have characterized the ion conduction properties of the first activation step by noise analysis and observed very similar behavior as in the two previously investigated concatemers (Fig. 6 H). Our experiments on WT_E702Q thus provide strong additional evidence for a predominantly in-

dependent activation of two separate ion conduction pores in the dimeric mTMEM16A channel. Although we cannot exclude the presence of weak coupling between the two subunits, our data are not detailed enough to permit such analysis.

Effect of a putative pore mutation

Finally, to further support the functional independence of two separate ion conduction pores contained in the dimeric protein, we were interested in changing the ion permeation properties of one subunit by introducing a mutation outside the calcium-binding site. We thus turned our attention toward Lys588, which, upon mutation to Gln, was previously suggested to lower the anion selectivity of mTMEM16A (Yang et al., 2012). In an attempt to enhance the effect of the mutation, we replaced the positively charged lysine with a negatively charged glutamate. Patch-clamp experiments of the single mutant K588E showed very low currents evoked in response to Ca^{2+} at concentrations that fully activate WT (Fig. 7 A). Nonstationary noise analysis indicates that the mutant has likely reduced γ and P_O, but, because the experimental variance–mean current relation has not reached a maximum, these values are, in this case, only a crude estimate (Fig. 7 A). Because of the low magnitude of the calcium-activated currents, we were not able to reliably characterize the ion selectivity of this mutant. In contrast to K588E, the double mutant K588E/E702Q showed robust currents at high Ca^{2+} concentrations, although with a pronounced outward rectification, which probably reflects a change in pore conductance as rectification is instantaneous and the current showed no time dependence in response to voltage jumps (Fig. 7 B). With respect to potency and voltage dependence, the Ca^{2+} dose–response relationships of this double mutant resemble E702Q (Fig. 7 C and Table 1). The characterization of outward currents by nonstationary noise analysis indicates similar properties as WT and E702Q (Fig. 7 D). The current of this double mutant also reverses close to the Nernst potential of Cl^-, indicating that the mutation did not affect the high anion selectivity observed in all investigated constructs (Fig. 7 E). The strong outward rectification but unchanged anion selectivity suggests that the residue may influence the access of anions from the intracellular side presumably by a electrostatic mechanism, akin to a Lys residue identified in the chloride channel CLC-0 (Chen and Chen, 2003). We have subsequently

(F) Rundown-corrected concentration–response relation of the WT_E702Q concatemer at 80 mV (n = 8–18 for each data point). The solid line is the best fit to the triphasic Hill equation. Dashed lines indicate the fist activation of WT (green) and E702Q (orange) at 80 mV. (G) Rundown-corrected concentration–response relations of the WT_E702Q concatemer at 80 and −80 mV (n = 8–18 for each data point). Lines are the best fit to a triphasic Hill equation. (H) Merged and averaged variance-<I> plot and pooled data (n = 9) of the WT_E702Q concatemer obtained at 2 µM $[Ca^{2+}]_{free}$ at 80 mV. (D and H, left) The dotted lines indicate the mean $P_{O\ max}$ across patches. (D and H, right) Dotted lines indicate the corresponding value of WT mTMEM16A. In B–D and F–H, data are presented as mean and errors as SEM.

A

K588E
2 μM Ca^{2+}

B

K588E/E702Q

C

K588E/E702Q

D

K588E/E702Q
1 mM Ca^{2+}

E

K588E/E702Q
1 mM Ca^{2+}

F

K588E_E702Q

G

WT_K588E/E702Q

H

I

K588E_E702Q

J

WT_K588E/E702Q

Independent activation of TMEM16A subunits | Lim et al.

prepared two chimeric constructs, one where we have introduced the mutation K588E in the WT subunit (K588E_E702Q) and another where we have introduced the mutation in the E702Q subunit (WT_K588E/E702Q). When studying the activation properties of the two concatemers (Fig. 7, F and G), both constructs show a phenotype that is consistent with the behavior of the involved subunits. In K588E_E702Q, the magnitude of the first activation at low Ca^{2+} concentration is small (accounting for 1.5% of the maximum response), consistent with the low currents observed in K588E, whereas the second, much larger activation step proceeds with a similar EC_{50} and Hill slope as expected for E702Q (Fig. 7 G and Table 1). In the mutant WT_K588E/E702Q, activation of both subunits proceeds with the expected Ca^{2+} dependence, but the second activation step in this case accounts for ∼60% of the maximum currents compared with the ∼70% in WT_E702Q when fitted to a biphasic Hill equation (Fig. 7 H and Table 1). This fraction decreases further when taking the biphasic activation of WT into account. In each of the two constructs, both activation steps have retained their voltage dependence, but because of the strong outward rectification of the currents mediated by the subunit containing the K588E mutation, the relative contribution of the K588E-containing subunit to the total current decreases at negative voltages (Fig. 7, I and J; and Table 1). This causes the first component to disappear in K588E_E702Q (Fig. 7 I) and to increase in WT_K588E/E702Q (Fig. 7 J). Our data thus demonstrate that, besides the activation by Ca^{2+}, the functional independence also extends to the conduction properties of the two ion permeation pores.

DISCUSSION

In our study, we have investigated the question of whether TMEM16A contains two separate ion conduction pores that are independently activated by Ca^{2+}. This question was motivated by the structure of nhTMEM16, a family member that works as lipid scramblase and contains two putative sites of catalysis on the opposite ends of a dimeric protein (Fig. 1; Brunner et al., 2014, 2016). We have initially studied the properties of WT in a broad range of Ca^{2+} concentrations and found a biphasic opening with a larger component at submicromolar and a second, smaller component, at low millimolar concentrations. The first activation step was described previously (Arreola et al., 1996; Kuruma and Hartzell, 2000). It is cooperative, voltage dependent, and likely accounts for the binding of Ca^{2+} to a site buried within the membrane domain that was identified in the structure of nhTMEM16 (Fig. 8; Brunner et al., 2014). The second activation lacks any voltage dependence and might thus reflect the interaction of Ca^{2+} with an unknown low-affinity site located at the cytoplasmic part of the channel. Because of its low apparent affinity, it is unlikely that the second activation plays a functional role in the physiological context, but it is important for the investigation of heterodimers with different activation properties described in this study. Our results suggest that exposure to 1 mM Ca^{2+} did not change the high anion over cation selectivity of the channel, nor its conductance, but that it results from an increase in the open probability (Fig. 3, C and D). This argues against a proposed transition into a different conducting conformation at high Ca^{2+} concentrations (Kuruma and Hartzell, 2000; Schroeder et al., 2008).

The investigation of a concatenated channel containing two WT subunits showed very similar properties, underlining that the covalent linkage did not strongly affect channel function (Fig. 4). By investigating the properties of concatenated dimers containing subunits with distinct activation and ion conduction properties, we could demonstrate that both subunits act independently with respect to their ion permeation and gat-

Figure 7. **Functional properties of the K588E_E702Q and the WT_K588E/E702Q concatemers.** (A) Merged and averaged variance-<I> plot and pooled data ($n = 5$) of the K588E mutant obtained at 2 µM $[Ca^{2+}]_{free}$ at 80 mV. (B, left) Representative currents of the K588E/E702Q double mutant at 80 and −80 mV. (right) I-V plots recorded at symmetrical 150 mM NaCl for WT ($n = 8$) and the K588E/E702Q double mutant ($n = 13$) at 1 mM $[Ca^{2+}]_{free}$. (C) Rundown-corrected concentration–response relations of the K588E/E702Q double mutant at 80 and −80 mV ($n = 10$ for each data point). Solid lines are the best fit to the Hill equation. Dashed lines indicate the relations of E702Q at 80 and −80 mV. (D) Merged and averaged variance-<I> plot and pooled data ($n = 9$) of the K588E/E702Q double mutant obtained at 1 mM $[Ca^{2+}]_{free}$ at 80 mV. (A [middle] and D [left]) The dotted lines indicate the mean $P_{O\ max}$ across patches. (A and D, right) Dotted lines indicate the corresponding value of WT mTMEM16A. (E) Na^+ versus Cl^- selectivity of the K588E/E702Q double mutant. (left) I-V plots recorded at 150 mM extracellular and the indicated intracellular NaCl concentrations at 1 mM ($n = 7$–13) $[Ca^{2+}]_{free}$. (right) Relation between intracellular [NaCl] and E_{rev} at 1 mM ($n = 7$–13) $[Ca^{2+}]_{free}$. The line indicates the Nernst potentials of Cl^-. (F) Representative currents of the K588E_E702Q concatemer at 80 and −80 mV. (G) Representative currents of the WT_K588E/E702Q concatemer at 80 and −80 mV. (B, F, and G) Blue and red dots indicate the reference pulses used for rundown correction at 80 and −80 mV, respectively (see Materials and methods). (H) Rundown-corrected concentration–response relation of the K588E_E702Q ($n = 7$–19 for each data point) and WT_K588E/E702Q ($n = 10$–21 for each data point) concatemer at 80 mV. Solid lines are the best fit to a biphasic Hill equation. Dashed line indicates the relation of the WT_E702Q concatemer at 80 mV. (I) Rundown-corrected concentration–response relations of the K588E_E702Q concatemer at 80 and −80 mV ($n = 7$–19 for each data point). Lines are the best fit to biphasic (80 mV) and monophasic (−80 mV) equations. (J) Rundown-corrected concentration–response relations of the WT_K588E/E702Q concatemer at 80 and −80 mV ($n = 10$–21 for each data point). Lines are the best fit to a biphasic Hill equation. In A–E and H–J, data are presented as mean and errors as SEM.
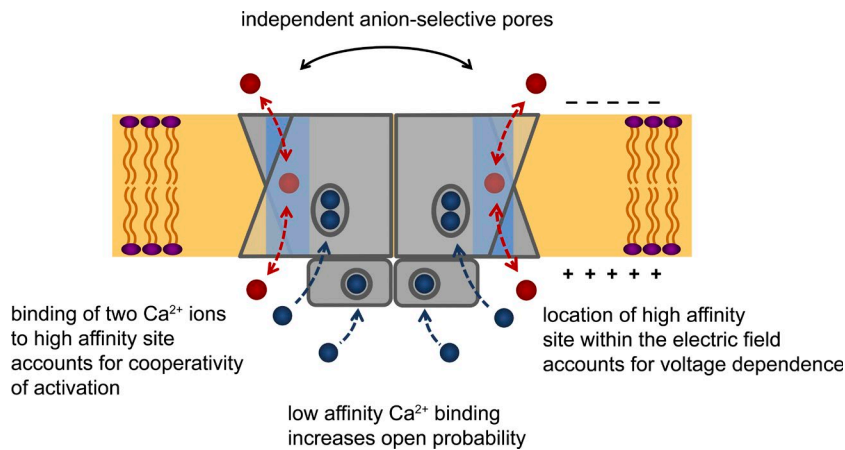
Figure 8. **Properties of TMEM16A.** Scheme summarizing the functional properties of TMEM16A. Ion conduction pores in the dimeric protein are indicated in light blue, Ca^{2+} is displayed as dark blue, and Cl^- is displayed as red spheres.

ing characteristics. We show that Ca^{2+} activates the WT subunit in a concatemer containing a second subunit with strongly impaired activation in a biphasic manner with similar potency and cooperativity as WT (Fig. 5). This implies that the biphasic opening is a property of the single subunit, and it suggests that the mutated subunit does not appreciably contribute to the currents induced at high Ca^{2+} concentrations. The cooperativity of the first transition underlines that the binding of the ligand to sites located within each subunit accounts for pore opening and that this process involves more than a single ion (Fig. 8). Our findings are thus consistent with the structure of nhTMEM16 where each binding site coordinates two Ca^{2+} ions (Brunner et al., 2014). The unchanged voltage dependence of Ca^{2+} activation in this construct supports the hypothesis that this phenomenon originates from the localization of the binding site within the transmembrane electric field (Brunner et al., 2014). Finally, the unaltered anion selectivity and conductance of the construct containing only a single activatable subunit provides additional evidence for the spatial separation of both pores. Functional independence is also supported by experiments on constructs where two subunits show different potency of activation and where each activation step retains the signature of the nonconcatenated counterparts. This is the case for a concatenated channel containing a mutation in the Ca^{2+}-binding site of one subunit that results in a more than 100-fold decrease in potency, and it extends to similar constructs containing an additional mutation that affects the ion conduction properties of the channel. Our data thus strongly suggest that, similar to the ClC family (Ludewig et al., 1996; Middleton et al., 1996; Dutzler et al., 2002, 2003), the dimeric TMEM16A channel contains two separate ion conduction pores. Similar to the fast gating of the channel CLC-0, the activation of a single pore is to a large degree independent, although we cannot exclude weak cross-talk between subunits, which might have escaped our detection.

The functional independence of both pores underlines the assumption that the nhTMEM16 structure displays the general architecture for both functional branches of the family (Fig. 1). In this respect, questions addressing the molecular features that distinguish scramblases from channels become even more important. Recently, it was shown that lipid scrambling could be conferred to TMEM16A by replacing a short stretch of amino acids of the protein lining the intracellular entrance of the subunit cavity by its equivalent sequence of the scramblase TMEM16F (Yu et al., 2015). This implies that the CaCCs of the TMEM16 family might have evolved from ancestral scramblases and that, different from other ion channel families, part of the ion conduction pore of TMEM16A may be lined by lipids (Whitlock and Hartzell, 2016). It is thus remarkable that such an unconventional ion channel has gained a central role in many physiologically relevant processes, which are otherwise mediated by proteins that have evolved for conducting ions from the outset of their functional emergence.

ACKNOWLEDGMENTS

REFERENCES

Arreola, J., J.E. Melvin, and T. Begenisich. 1996. Activation of calcium-dependent chloride channels in rat parotid acinar cells. *J. Gen. Physiol.* 108:35–47. http://dx.doi.org/10.1085/jgp.108.1.35

Brunner, J.D., N.K. Lim, S. Schenck, A. Duerst, and R. Dutzler. 2014. X-ray structure of a calcium-activated TMEM16 lipid scramblase. *Nature.* 516:207–212. http://dx.doi.org/10.1038/nature13984

Brunner, J.D., S. Schenck, and R. Dutzler. 2016. Structural basis for phospholipid scrambling in the TMEM16 family. *Curr. Opin. Struct. Biol.* 39:61–70. http://dx.doi.org/10.1016/j.sbi.2016.05.020

Caputo, A., E. Caci, L. Ferrera, N. Pedemonte, C. Barsanti, E. Sondo, U. Pfeffer, R. Ravazzolo, O. Zegarra-Moran, and L.J. Galietta. 2008. TMEM16A, a membrane protein associated with calcium-dependent chloride channel activity. *Science.* 322:590–594. http://dx.doi.org/10.1126/science.1163518

Chen, C., and H. Okayama. 1987. High-efficiency transformation of mammalian cells by plasmid DNA. *Mol. Cell. Biol.* 7:2745–2752. http://dx.doi.org/10.1128/MCB.7.8.2745

Chen, M.F., and T.Y. Chen. 2003. Side-chain charge effects and conductance determinants in the pore of ClC-0 chloride channels. *J. Gen. Physiol.* 122:133–145. http://dx.doi.org/10.1085/jgp.200308844

Doyle, D.A., J. Morais Cabral, R.A. Pfuetzner, A. Kuo, J.M. Gulbis, S.L. Cohen, B.T. Chait, and R. MacKinnon. 1998. The structure of the potassium channel: molecular basis of K^+ conduction and selectivity. *Science.* 280:69–77. http://dx.doi.org/10.1126/science.280.5360.69

Dutzler, R., E.B. Campbell, M. Cadene, B.T. Chait, and R. MacKinnon. 2002. X-ray structure of a ClC chloride channel at 3.0 Å reveals the molecular basis of anion selectivity. *Nature.* 415:287–294. http://dx.doi.org/10.1038/415287a

Dutzler, R., E.B. Campbell, and R. MacKinnon. 2003. Gating the selectivity filter in ClC chloride channels. *Science.* 300:108–112. http://dx.doi.org/10.1126/science.1082708

Ferrera, L., A. Caputo, I. Ubby, E. Bussani, O. Zegarra-Moran, R. Ravazzolo, F. Pagani, and L.J. Galietta. 2009. Regulation of TMEM16A chloride channel properties by alternative splicing. *J. Biol. Chem.* 284:33360–33368. http://dx.doi.org/10.1074/jbc.M109.046607

Geertsma, E.R., and R. Dutzler. 2011. A versatile and efficient high-throughput cloning tool for structural biology. *Biochemistry.* 50:3272–3278. http://dx.doi.org/10.1021/bi200178z

Hamill, O.P., A. Marty, E. Neher, B. Sakmann, and F.J. Sigworth. 1981. Improved patch-clamp techniques for high-resolution current recording from cells and cell-free membrane patches. *Pflugers Arch.* 391:85–100. http://dx.doi.org/10.1007/BF00656997

Hartzell, C., I. Putzier, and J. Arreola. 2005. Calcium-activated chloride channels. *Annu. Rev. Physiol.* 67:719–758. http://dx.doi.org/10.1146/annurev.physiol.67.032003.154341

Heinemann, S.H., and F. Conti. 1992. Nonstationary noise analysis and application to patch clamp recordings. *Methods Enzymol.* 207:131–148. http://dx.doi.org/10.1016/0076-6879(92)07009-D

Huang, F., X. Wong, and L.Y. Jan. 2012. International Union of Basic and Clinical Pharmacology. LXXXV: Calcium-activated chloride channels. *Pharmacol. Rev.* 64:1–15. http://dx.doi.org/10.1124/pr.111.005009

Jeng, G., M. Aggarwal, W.-P. Yu, and T.-Y. Chen. 2016. Independent activation of distinct pores in dimeric TMEM16A channels. *J. Gen. Physiol.* http://dx.doi.org/10.1085/jgp.201611651

Kunzelmann, K., P. Kongsuphol, F. Aldehni, Y. Tian, J. Ousingsawat, R. Warth, and R. Schreiber. 2009. Bestrophin and TMEM16-Ca^{2+} activated Cl^- channels with different functions. *Cell Calcium.* 46:233–241. http://dx.doi.org/10.1016/j.ceca.2009.09.003

Kuruma, A., and H.C. Hartzell. 2000. Bimodal control of a Ca^{2+}-activated Cl^- channel by different Ca^{2+} signals. *J. Gen. Physiol.* 115:59–80. http://dx.doi.org/10.1085/jgp.115.1.59

Ludewig, U., M. Pusch, and T.J. Jentsch. 1996. Two physically distinct pores in the dimeric ClC-0 chloride channel. *Nature.* 383:340–343. http://dx.doi.org/10.1038/383340a0

Malvezzi, M., M. Chalat, R. Janjusevic, A. Picollo, H. Terashima, A.K. Menon, and A. Accardi. 2013. Ca^{2+}-dependent phospholipid scrambling by a reconstituted TMEM16 ion channel. *Nat. Commun.* 4:2367. http://dx.doi.org/10.1038/ncomms3367

Middleton, R.E., D.J. Pheasant, and C. Miller. 1996. Homodimeric architecture of a ClC-type chloride ion channel. *Nature.* 383:337–340. http://dx.doi.org/10.1038/383337a0

Miller, C. 1982. Open-state substructure of single chloride channels from Torpedo electroplax. *Philos. Trans. R. Soc. Lond. B Biol. Sci.* 299:401–411. http://dx.doi.org/10.1098/rstb.1982.0140

Miyazawa, A., Y. Fujiyoshi, and N. Unwin. 2003. Structure and gating mechanism of the acetylcholine receptor pore. *Nature.* 423:949–955. http://dx.doi.org/10.1038/nature01748

Ni, Y.L., A.S. Kuan, and T.Y. Chen. 2014. Activation and inhibition of TMEM16A calcium-activated chloride channels. *PLoS One.* 9:e86734. http://dx.doi.org/10.1371/journal.pone.0086734

Pedemonte, N., and L.J. Galietta. 2014. Structure and function of TMEM16 proteins (anoctamins). *Physiol. Rev.* 94:419–459. http://dx.doi.org/10.1152/physrev.00039.2011

Peters, C.J., H. Yu, J. Tien, Y.N. Jan, M. Li, and L.Y. Jan. 2015. Four basic residues critical for the ion selectivity and pore blocker sensitivity of TMEM16A calcium-activated chloride channels. *Proc. Natl. Acad. Sci. USA.* 112:3547–3552. http://dx.doi.org/10.1073/pnas.1502291112

Picollo, A., M. Malvezzi, and A. Accardi. 2015. TMEM16 proteins: unknown structure and confusing functions. *J. Mol. Biol.* 427:94–105. http://dx.doi.org/10.1016/j.jmb.2014.09.028

Portolano, N., P.J. Watson, L. Fairall, C.J. Millard, C.P. Milano, Y. Song, S.M. Cowley, and J.W. Schwabe. 2014. Recombinant protein expression for structural biology in HEK 293F suspension cells: a novel and accessible approach. *J. Vis. Exp.* (92):e51897.

Qu, Z., and H.C. Hartzell. 2000. Anion permeation in Ca^{2+}-activated Cl^- channels. *J. Gen. Physiol.* 116:825–844. http://dx.doi.org/10.1085/jgp.116.6.825

Schroeder, B.C., T. Cheng, Y.N. Jan, and L.Y. Jan. 2008. Expression cloning of TMEM16A as a calcium-activated chloride channel subunit. *Cell.* 134:1019–1029. http://dx.doi.org/10.1016/j.cell.2008.09.003

Sigworth, F.J. 1980. The variance of sodium current fluctuations at the node of Ranvier. *J. Physiol.* 307:97–129. http://dx.doi.org/10.1113/jphysiol.1980.sp013426

Suzuki, J., M. Umeda, P.J. Sims, and S. Nagata. 2010. Calcium-dependent phospholipid scrambling by TMEM16F. *Nature.* 468:834–838. http://dx.doi.org/10.1038/nature09583

Suzuki, J., T. Fujii, T. Imao, K. Ishihara, H. Kuba, and S. Nagata. 2013. Calcium-dependent phospholipid scramblase activity of TMEM16 protein family members. *J. Biol. Chem.* 288:13305–13316. http://dx.doi.org/10.1074/jbc.M113.457937

Ta, C.M., A. Adomaviciene, N.J. Rorsman, H. Garnett, and P. Tammaro. 2016. Mechanism of allosteric activation of TMEM16A/ANO1 channels by a commonly used chloride channel blocker. *Br. J. Pharmacol.* 173:511–528. http://dx.doi.org/10.1111/bph.13381

Terashima, H., A. Picollo, and A. Accardi. 2013. Purified TMEM16A is sufficient to form Ca^{2+}-activated Cl^- channels. *Proc. Natl. Acad. Sci. USA.* 110:19354–19359. http://dx.doi.org/10.1073/pnas.1312014110

Tien, J., C.J. Peters, X.M. Wong, T. Cheng, Y.N. Jan, L.Y. Jan, and H. Yang. 2014. A comprehensive search for calcium binding sites critical for TMEM16A calcium-activated chloride channel activity. *eLife.* 3:e02772. http://dx.doi.org/10.7554/eLife.02772

Whitlock, J.M., and H.C. Hartzell. 2016. A Pore Idea: the ion conduction pathway of TMEM16/ANO proteins is composed partly of lipid. *Pflugers Arch.* 468:455–473. http://dx.doi.org/10.1007/s00424-015-1777-2

Xiao, Q., K. Yu, P. Perez-Cornejo, Y. Cui, J. Arreola, and H.C. Hartzell. 2011. Voltage- and calcium-dependent gating of TMEM16A/Ano1 chloride channels are physically coupled by the first intracellular loop. *Proc. Natl. Acad. Sci. USA.* 108:8891–8896. http://dx.doi.org/10.1073/pnas.1102147108

Yang, H., A. Kim, T. David, D. Palmer, T. Jin, J. Tien, F. Huang, T. Cheng, S.R. Coughlin, Y.N. Jan, and L.Y. Jan. 2012. TMEM16F forms a Ca^{2+}-activated cation channel required for lipid scrambling in platelets during blood coagulation. *Cell.* 151:111–122. http://dx.doi.org/10.1016/j.cell.2012.07.036

Yang, Y.D., H. Cho, J.Y. Koo, M.H. Tak, Y. Cho, W.S. Shim, S.P. Park, J. Lee, B. Lee, B.M. Kim, et al. 2008. TMEM16A confers receptor-activated calcium-dependent chloride conductance. *Nature.* 455:1210–1215. http://dx.doi.org/10.1038/nature07313

Yu, K., C. Duran, Z. Qu, Y.Y. Cui, and H.C. Hartzell. 2012. Explaining calcium-dependent gating of anoctamin-1 chloride channels requires a revised topology. *Circ. Res.* 110:990–999. http://dx.doi.org/10.1161/CIRCRESAHA.112.264440

Yu, K., J.M. Whitlock, K. Lee, E.A. Ortlund, Y.Y. Cui, and H.C. Hartzell. 2015. Identification of a lipid scrambling domain in ANO6/TMEM16F. *eLife.* 4:e06901. http://dx.doi.org/10.7554/eLife.06901